High-resolution structures of HIV-1 Gag cleavage mutants determine structural switch for virus maturation

Simone Mattei[a,b,c,1], Aaron Tan[a,b,d,e,1,2], Bärbel Glass[f], Barbara Müller[b,f], Hans-Georg Kräusslich[b,f,3], and John A. G. Briggs[a,b,d,3]

[a]Structural and Computational Biology Unit, European Molecular Biology Laboratory (EMBL), 69117 Heidelberg, Germany; [b]Molecular Medicine Partnership Unit, EMBL and Universitätsklinikum Heidelberg, 69117 Heidelberg, Germany; [c]Institute of Molecular Biology and Biophysics, ETH Zürich, 8093 Zürich, Switzerland; [d]Structural Studies Division, Medical Research Council Laboratory of Molecular Biology, Cambridge CB2 0QH, United Kingdom; [e]Faculty of Biosciences, Heidelberg University, 69120 Heidelberg, Germany; and [f]Department of Infectious Diseases, Virology, Universitätsklinikum Heidelberg, 69120 Heidelberg, Germany

Edited by John M. Coffin, Tufts University School of Medicine, Boston, MA, and approved August 8, 2018 (received for review June 29, 2018)

HIV-1 maturation occurs via multiple proteolytic cleavages of the Gag polyprotein, causing rearrangement of the virus particle required for infectivity. Cleavage results in beta-hairpin formation at the N terminus of the CA (capsid) protein and loss of a six-helix bundle formed by the C terminus of CA and the neighboring SP1 peptide. How individual cleavages contribute to changes in protein structure and interactions, and how the mature, conical capsid forms, are poorly understood. Here, we employed cryoelectron tomography to determine morphology and high-resolution CA lattice structures for HIV-1 derivatives in which Gag cleavage sites are mutated. These analyses prompt us to revise current models for the crucial maturation switch. Unlike previously proposed, cleavage on either terminus of CA was sufficient, in principle, for lattice maturation, while complete processing was needed for conical capsid formation. We conclude that destabilization of the six-helix bundle, rather than beta-hairpin formation, represents the main determinant of structural maturation.

retrovirus | capsid | cryoelectron tomography | maturation | subtomogram averaging

The major structural component of HIV-1 is the 55-kDa polyprotein Gag. Gag oligomerization at the plasma membrane of infected cells directs the budding and release of enveloped immature virus particles. The Gag proteins of all retroviruses include three conserved domains: the MA (matrix) domain, which binds the plasma membrane; the CA (capsid) domain, which, upon cleavage, forms the mature viral capsid; and the NC (nucleocapsid) domain, which packages the viral RNA genome into a ribonucleoprotein (RNP) complex. HIV-1 Gag comprises, in addition, a short spacer peptide between CA and NC called SP1 and two further peptides, SP2 and p6, downstream of NC (Fig. 1*A*). Gag is radially arranged in the immature virus particle with the N-terminal MA domain at the membrane and the C-terminal end of the protein pointing toward the center of the virus particle. Between them, the CA domain forms a hexameric protein lattice arranged as an incomplete sphere containing irregularly shaped defects. Concomitant with or shortly after budding, the viral protease (PR) cleaves Gag at five positions, separating it into its component domains and peptides, and leading to rearrangement of the virus into its mature, infectious form (Fig. 1*A*). The viral PR is expressed as part of the 160-kDa Gag-Pol polyprotein, which is produced by a ribosomal frameshift and incorporated into the immature lattice at ∼5% abundance. In the mature virus particle, MA is believed to remain associated with the membrane; CA forms the cone-shaped mature capsid core; and NC, together with the viral RNA, forms a condensed RNP complex within the capsid (1–5).

The structures of both immature and mature HIV-1 particles have been extensively studied by cryoelectron tomography (cryo-ET) and subtomogram averaging (6–11), as well as by crystallography of purified protein components and multimers thereof (12–17). These studies have led to atomic models of the CA domain within the assembled Gag lattice of immature viruses (10, 17) and in mature viral capsids (11, 16) that reveal the networks of interactions that stabilize the CA domain lattice. In both cases, CA assembles a hexameric protein lattice, but the hexamer–hexamer spacing differs (18, 19) and the CA–CA interfaces that mediate interactions within the lattice are almost completely nonoverlapping (20). Some disassembly and reassembly of the interactions of the CA N-terminal domain (CA-NTD) and CA C-terminal domain (CA-CTD) are therefore required during maturation. Upon cleavage, the N terminus of the CA-NTD folds down upon itself to form a beta-hairpin (21). Downstream of the CA-CTD, an alpha-helix that crosses the CA-SP1 boundary forms a six-helix bundle in the immature lattice (10, 17, 22) that is disassembled upon maturation, and the C-terminal part of CA is disordered in the mature lattice. Maturation is therefore associated with dramatic changes in CA structure, particularly at the termini of the protein, as well as changes in CA arrangement (reviewed in ref. 5) (Movie S1).

Significance

The main structural component of HIV-1 is the Gag polyprotein. During virus release, Gag is cleaved by the viral protease at five sites, triggering a major change in the structure and morphology of the virus. This transition, called maturation, is required to make an infectious virion. We used cryoelectron tomography to obtain high-resolution structures of Gag inside virus particles carrying mutations that block specific combinations of cleavage sites. Analysis of these structures suggests that different combinations of cleavages can destabilize a bundle of alpha-helices at the C terminus of CA. This destabilization, rather than formation of a beta-hairpin at the N terminus of CA as previously suggested, acts as the structural switch for maturation of the virus into its infectious form.

Author contributions: H.-G.K. and J.A.G.B. designed research; S.M., A.T., and B.G. performed research; S.M., A.T., H.-G.K., and J.A.G.B. analyzed data; and S.M., A.T., B.M., H.-G.K., and J.A.G.B. wrote the paper.

The authors declare no conflict of interest.

This article is a PNAS Direct Submission.

Data deposition: The structures described in this paper have been deposited in the Electron Microscopy Data Bank (www.ebi.ac.uk/pdbe/emdb) under accession codes EMD-0164–EMD-0171.

[1]S.M. and A.T. contributed equally to this work.

[2]Candidate for joint PhD degree between EMBL and Faculty of Biosciences, Heidelberg University.

[3]To whom correspondence may be addressed. Email: hans-georg.kraeusslich@med.uni-heidelberg.de or jbriggs@mrc-lmb.cam.ac.uk.

This article contains supporting information online at www.pnas.org/lookup/suppl/doi:10.1073/pnas.1811237115/-/DCSupplemental.

Published online September 14, 2018.

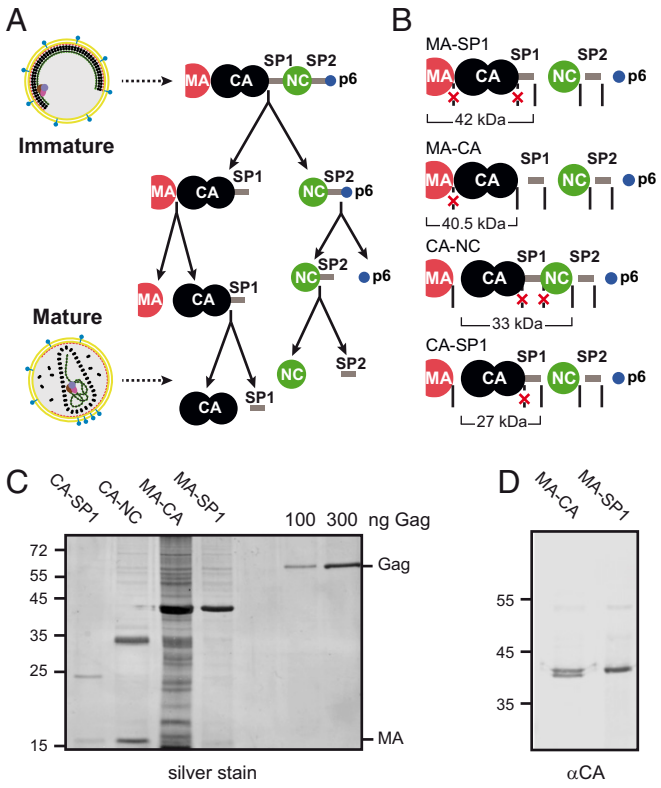

Fig. 1. Biochemical characterization of mutant virus-like particles used in this study. (*A*) Schematic illustration of the proteolytic cleavages involved in HIV-1 Gag maturation, ordered by relative rate as determined using purified PR in solution (23). Schematic representations of typical immature and mature viral morphologies are displayed to the left of the corresponding stages in the proteolytic cleavage cascade. (*B*) Schematic representation of Gag cleavage patterns in each of the cleavage mutants used. Mutated sites that cannot be cleaved are denoted with crossed out, dashed lines. Sites where cleavage occurs as in wild-type Gag are denoted by solid lines. Brackets under the schematics indicate the CA-containing products that remain unprocessed and their corresponding molecular mass. (*C*) SDS/PAGE analysis of virus preparations used for the structural analyses. Particles were purified from the supernatant of transfected HEK293T cells by ultracentrifugation through an iodixanol gradient. Samples were separated by SDS/PAGE (12.5% acrylamide, 30:1 acrylamide/bisacrylamide), and proteins were visualized by silver staining. Numbers to the left indicate the position of molecular mass standards (in kilodaltons). Purified recombinant Gag protein was used as a standard to estimate particle concentration. (*D*) Quantitative immunoblot analysis of MA-CA and MA-SP1 band intensities. Samples were separated by SDS/PAGE (12% acrylamide, 200:1 acrylamide/bisacrylamide), and proteins were detected by quantitative immunoblot (LI-COR Biotechnology) using a polyclonal antiserum raised against recombinant CA.

Despite the availability of detailed models for the immature and mature states, little is known about the intermediate states of HIV-1 maturation. The cleavages that release the domains of Gag proceed at very different rates, influenced by protein sequence and structure. In vitro, cleavage rates for different sites on the Gag polyprotein vary by a factor of ∼400. Cleavage occurs fastest at the SP1-NC cleavage site, followed by SP2-p6, MA-CA, NC-SP2, and, finally, CA-SP1 (23). Within the virus, computational models indicate that during the cleavage cascade, different sites are being cleaved in different Gag molecules at the same time (24). Interfering with cleavage at individual sites is disruptive to morphological maturation (22, 25–32).

We have previously investigated the structure of the CA layer in HIV-1 variants carrying combinations of cleavage site mutations within Gag to prevent cleavage at specific sites (30). These virus derivatives were named according to the CA-containing polypeptide present after proteolytic processing and included MA-SP1, MA-CA, CA-SP1, and CA-p6 (Fig. 1*B*). By determining low-resolution structures of the CA domain in each of these variants by cryo-ET and subtomogram averaging, we found that the immature lattice only disassembled in the case of CA-SP1, but remained intact when cleavage at either side of the CA-SP1 module was prevented. We concluded that combined cleavage both upstream of CA and downstream of the CA-SP1 module is required to destabilize the immature Gag lattice, and thus permit maturation (30). Once the immature lattice has been destabilized, the lower energy mature-like state is favored. When assembled in vitro, bypassing the immature state, CA, CA-SP1, and CA-NC constructs all preferentially assemble mature-like lattices (21, 33–35).

Despite this progress, many open questions remain about the mechanism of HIV-1 maturation. Does beta-hairpin formation or CA-SP1 helix disordering, or both, represent a structural switch that regulates maturation or a structural change that results from maturation? How do cleavages upstream and downstream of CA-SP1 together modulate the immature structure and lead to disassembly? What are the roles of individual cleavages? What do maturation intermediates look like?

Here, we have assessed the morphology of hundreds of virus particles, each from a panel of HIV-1 variants with cleavage site mutations, and have determined structures of their respective CA domain lattices at high resolution. These data allow minority phenotypes to be identified and local protein secondary structure to be resolved. Contrary to our previous results, this more detailed analysis revealed that cleavage on only one side of CA-SP1 can be sufficient to permit formation of the mature lattice and determined that CA-SP1 helix disordering, but not beta-hairpin formation, is a structural switch for HIV-1 maturation.

Results

Virus-like particles giving rise to the variants MA-SP1, MA-CA, CA-NC, and CA-SP1, respectively, were produced by transfection of subviral plasmids into HEK293T cells and purified as described previously (30). As described previously, all variants are noninfectious. Purity of particle preparations and Gag processing state were assessed by SDS/PAGE and quantitative immunoblot analysis of particle lysates using antibodies against CA (Fig. 1 *C* and *D*). In all cases, the expected cleavage products were observed. As we had noted earlier (30), cleavage between CA and SP1 was incomplete in case of the MA-CA variant, occurring with roughly 50% efficiency in the preparation analyzed here (Fig. 1*D*). In the following, we first describe the overall morphology of the Gag lattice in the different variants; then, the high-resolution structures of the immature- and/or mature-like CA lattice observed in these particles; and, finally, the architecture of the capsid structures that were formed.

Morphology of the Gag Lattice in Cleavage Site Defective Particles. Purified particles were vitrified by plunge-freezing, and their morphology was assessed by cryo-ET. Acquisition parameters for all variant particles are summarized in Table 1. At least 350 virus particles were imaged for all variants previously described as having immature-like morphology (MA-SP1, MA-CA, and CA-NC). For CA-SP1, 103 virus particles were imaged. Recent technical advances in cryo-ET (36) allowed us to generate higher quality tomograms, and to obtain approximately sevenfold larger datasets, than was possible in our earlier work (30), revealing the presence of minority phenotypes (Fig. 2 *B*, *ix* and *x*, and C, *xiv* and *xv*).

As described previously (30), MA-SP1 particles displayed a striated layer beneath the viral membrane typical of the immature HIV-1 CA layer (Fig. 2 *A*, *i*–*v*). Two percent (seven of 362) of virus particles displayed radially arranged densities corresponding to both CA and NC, indicating that they are fully immature and have not undergone proteolytic cleavage (Fig. 2 *A*, *i*). Ninety-eight percent (355 of 362) of particles lacked the innermost NC ring (Fig. 2 *A*, *ii*–*v*), consistent with proteolytic cleavage having occurred between CA and NC. Eighty-eight percent (310 of 355) of

Table 1. Summary of data acquisition parameters for all cleavage mutants

Parameter, units	Sample			
	HIV-1 MA-SP1	HIV-1 MA-CA	HIV-1 CA-SP1	HIV-1 CA-NC
Microscope	FEI Titan Krios	FEI Titan Krios	FEI Titan Krios	FEI Titan Krios
Voltage, keV	300	300	300	300
Detector	Gatan Quantum K2	Gatan Quantum K2	Gatan Quantum K2	Gatan Quantum K2
Energy filter	Yes	Yes	Yes	Yes
Slit width, eV	20	20	20	20
Superresolution mode	Yes	Yes	Yes	Yes
Ångströms per pixel	1.35	1.35	1.35	1.35
Defocus range, μm	−1.5 to −5.0	−1.5 to −5.0	−2.0 to −4.0	−1.55 to −5.05
Defocus step, μm	0.25	0.25	0.25	0.25
Acquisition scheme	−60/60°, 3°, dose-symmetric	−60/60°, 3°, dose-symmetric	−60/60°, 3°, dose-symmetric	−60/60°, 3°, dose-symmetric
Total dose, electrons per $Å^2$	∼145	∼150	∼100	∼150
Dose rate, electrons per $Å^2 \cdot s^{-1}$	∼2.3	∼2.3	∼2.4	∼2.3
Frame number	10	21	5	20
Tomogram number	65	70	49	88

the particles that had undergone cleavage contained a condensed luminal density characteristic of condensed RNP (Fig. 2 *A*, *ii–iv*), as previously described for this variant (30).

In the MA-CA preparation, 3% (13 of 404) of particles had a fully immature phenotype (Fig. 2 *B*, *vi*), while 84% (341 of 404) of particles displayed the morphology previously described for this variant: a striated immature-like CA layer similar to that commonly observed in MA-SP1 (Fig. 2 *B*, *vii* and *viii*). The majority of these particles also contained a condensed RNP similar to MA-SP1 (discussed below). Eleven percent (45 of 404) of particles presented a CA layer that was thin, as is seen for the mature CA layer in wild-type HIV-1 virions (Fig. 2 *B*, *ix* and *x*). The majority of these particles (34 of 45) contained a mixture of mature-like (thin) and immature-like (thick) CA layers (Fig. 2 *B*, *ix*), while the remaining 11 particles appeared to contain only a mature-like thin CA lattice (Fig. 2 *B*, *x*). In all cases, the mature-like CA layer had not formed a conical capsid but, instead, was close to the membrane (Fig. 2 *B*, *ix* and *x*). In the 34 mixed-phenotype particles (Fig. 2 *B*, *ix*), the condensed RNP complex was always adjacent to the mature-like part of the lattice. The presence of thin mature-like CA layers in MA-CA suggests that complete or partial structural maturation of the CA layer can occur in a stochastic manner without cleavage between MA and CA.

In the majority of MA-CA and MA-SP1 particles, the immature CA layer (lacking the downstream RNP layer) had an architecture resembling a truncated sphere with a large gap. This architecture is typical of immature wild-type HIV-1 particles; the gap has been proposed to represent a budding scar (37). A smaller subset of particles carrying immature-like CA lattices displayed an almost complete spherical Gag shell with no large gap [31 of 355 for MA-SP1 (Fig. 2 *A*, *v*) and 19 of 341 for MA-CA (Fig. 2 *B*, *viii*)]. Many of these particles lacked a recognizable condensed RNP (19 of 31 for MA-SP1 and 16 of 19 for MA-CA). A similar phenotype (an almost complete spherical immature CA shell lacking RNP) had previously been observed for HIV-1 virus-like particles resulting from adenoviral vector-mediated expression of the wild-type HIV-1 Gag and Gag-Pol polyproteins (38). In this case, it was suggested to result from premature cleavage between SP1 and NC before budding, resulting in dissociation of the RNP away from the nascent bud and loss of the p6 domain responsible for endosomal sorting complex required for transport (ESCRT) recruitment. The absence of ESCRT recruitment may allow assembly of the immature lattice to continue to near completion. Occurrence of this phenotype for both MA-CA and MA-SP1 variants is consistent with the proposed premature cleavage occurring between SP1 and NC.

In the CA-NC preparation, 89% (319 of 357) of particles displayed a striated immature CA density that, in many cases, was slightly detached from the membrane (Fig. 2 *C*, *xi–xiii*), as was previously described for CA-p6 particles (30). Roughly 10% (35 of 357) of CA-NC particles contained a thin mature-like CA layer (Fig. 2 *C*, *xiv* and *xv*). Of these particles, 22 of 35 also contained partial immature-like CA layers, often adjacent to the mature-like parts of the CA lattice (Fig. 2 *C*, *xiv*), while 13 of 35 contained a thin, fully mature CA lattice (Fig. 2 *C*, *xv*). Mature-like CA lattices were underlined by an additional layer of density most likely corresponding to the NC-RNA layer. Mature-like CA lattices were more tightly curved than immature CA lattices, having curvatures similar to those seen in mature HIV-1 cores. The presence of a mature-like CA layer in the CA-NC variant suggests that complete or partial structural maturation of the CA layer can also occur without cleavage between CA and NC in a stochastic manner.

Consistent with previous observations (30, 39), the majority (78 of 103) of CA-SP1 particles displayed a thin layer of density, similar to the mature CA lattice, that formed irregular, open structures resembling partial polyhedra (Fig. 2 *D*, *xvii–xx*). Three percent (three of 103) of CA-SP1 particles appeared fully immature (Fig. 2 *D*, *xvi*), while the remaining 21% (22 of 103) of particles had no clear capsid layer. In most cases, the thin mature-like CA layer was closely apposed to the inner layer of the lipid envelope and no formation of cone-shaped capsids was observed.

Structural Analysis of Immature-Like Gag Lattices. The morphologies of the HIV-1 variants described above suggest that partial structural maturation can take place despite incomplete proteolytic cleavage of Gag. To confirm this conclusion, and to obtain detailed structural information, we applied subtomogram averaging to determine higher resolution structures of the immature CA lattices identified in MA-SP1, MA-CA, and CA-NC particles (Fig. 3). The three datasets were processed independently as described in *Materials and Methods* to yield structures of the CA-SP1 layer with resolutions of 4.0 Å, 3.7 Å, and 4.5 Å, respectively (*SI Appendix*, Fig. S1*A*). We then fitted the Protein Data Bank (PDB) model previously generated based on the 3.9-Å structure of the immature Gag layer in wild-type immature HIV-1 particles (PDB ID code 5L93) (10) to the variant CA-SP1 structures. In all cases the PDB model could be fitted as a rigid body, with excellent correspondence between the model and density throughout the ordered region of the CA-SP1 layer (*SI Appendix*, Fig. S2).

Residues N-terminal to helix 1 of the CA-NTD, including residues 133–145 (CA residues 1–13, which form the N-terminal beta-hairpin in fully processed CA), were poorly resolved in all of the variant structures, as previously described for wild-type immature HIV-1 (10) (Fig. 3*B*). This observation suggests flexibility in this

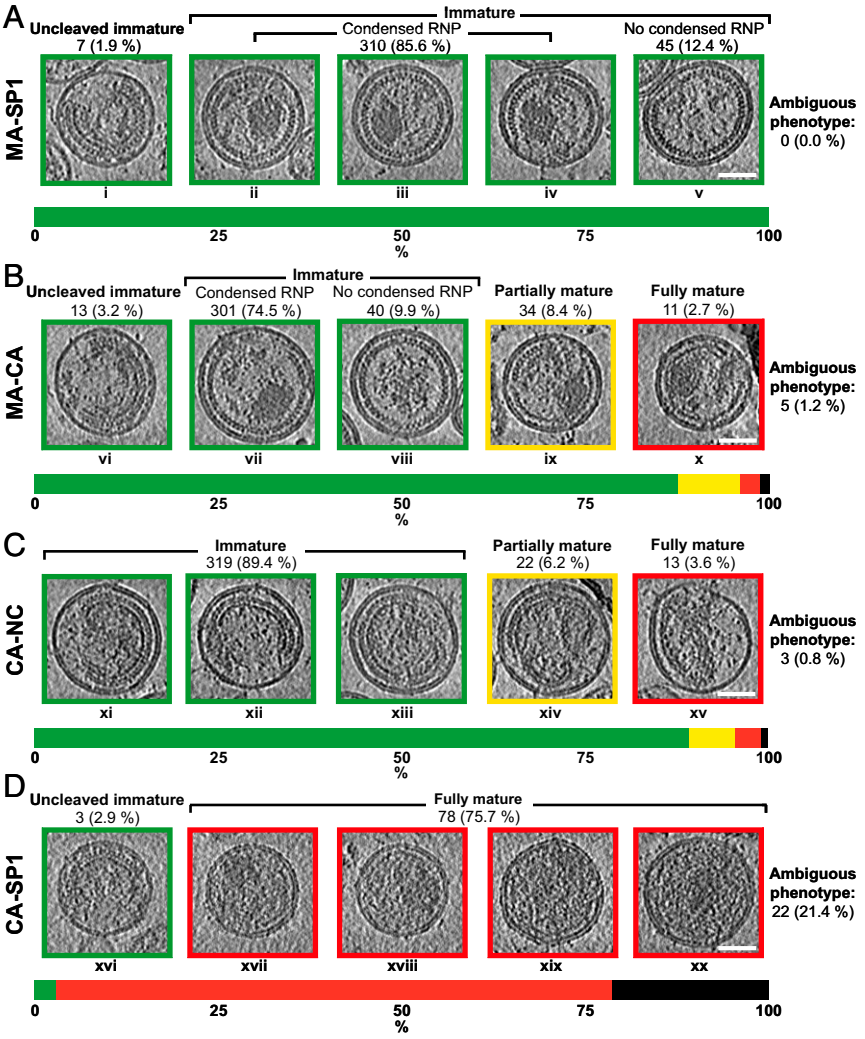

Fig. 2. (*A–D*, *i–xx*) Representative viral morphologies for each of the cleavage mutants. Orthoslices through tomograms show representative examples of the viral morphologies observed in the different datasets. The frequency of each phenotype in the corresponding dataset is shown above each of the panels, as well as the percentage of the respective dataset that each absolute frequency represents. Color bars underneath each set of orthoslices represent the percentage of viral particles displaying immature (green), partially mature (yellow), mature (red), or undefined (black) morphology. Scale bars, 50 nm.

region. We low-pass-filtered all structures to a resolution of 6 Å, allowing density N-terminal to helix 1 to be better resolved (Fig. 3*C*). In wild-type immature particles and in MA-SP1 and MA-CA variants, the resolved density corresponds approximately to Gag residues 143–149 (CA residues 11–17). In the CA-NC variant, this density was larger and wider than in the other cases. The size and shape of this density strongly suggest that the beta-hairpin has been formed within the immature Gag lattice in this case (Fig. 3*C*, *Right*), although the resolution achieved precludes a definitive statement.

The density resolved for the C-terminal CA-SP1 helix in wild-type immature HIV-1 extended to residue 371 of Gag (residue 8 of SP1) (10). This helix displayed the same length, with the same residues resolved, in the immature lattice of variants MA-SP1, MA-CA, and CA-NC (Fig. 3*D*), indicating that cleavage between SP1 and NC does not result in structural change in the CA-SP1 helical bundle when the MA-CA site remains uncleaved. MA-CA particle preparations contained a mixed population of MA-CA and MA-SP1 molecules, as shown by immunoblot, with ∼50% of molecules uncleaved at the CA-SP1 processing site (Fig. 1*D*). The distribution of cleaved and uncleaved molecules between individual particles or between hexamers within one particle cannot be derived from this bulk analysis, however. We observed no structural change in the helix for the MA-CA variant, despite partial removal of SP1.

Structural Analysis of Mature-Like Gag Lattices. We then applied subtomogram averaging to determine the structures of the mature-like CA lattices observed in MA-CA, CA-NC, and CA-SP1 particles at final resolutions of 8.3 Å, 9.7 Å, and 7.9 Å, respectively (Fig. 4 and *SI Appendix*, Fig. S1*B*). All three structures resembled that of the CA lattice determined in the mature wild-type HIV-1 capsid (11). They displayed the same arrangement of protein monomers within the lattice, suggesting that both intra- and interhexamer stabilizing interfaces are largely conserved in the variant particles (Fig. 4).

In the CA-NC structure, no density was seen for residues 354–378, corresponding to the helical region between the CA-CTD and NC (Fig. 4*B*). We conclude that the six-helix bundle observed in the immature lattice is absent in the mature CA-NC lattice, despite the abolition of cleavage between CA and SP1 and the presence of the SP1-NC regions downstream of CA.

The N-terminal beta-hairpin was clearly resolved in the CA-SP1 structure and appeared to adopt the closed conformation observed for the mature CA hexamer within wild-type capsids (11) (Fig. 4*B*). Density for the beta-hairpin was also visible for the CA-NC variant, but its conformation could not be reliably determined (Fig. 4*B*). In the MA-CA variant, formation of the beta-hairpin was prevented by covalent linkage of MA and CA. Consistently, we observed a much weaker density at the respective position compared with the other mature lattices (Fig. 4*B*); the observed density is likely to represent the initial residues of the linker connecting the CA-NTD to MA.

We next identified pentameric positions in the mature-like hexameric lattices of these variants, as we have previously described for wild-type mature HIV-1 capsids (11). For CA-SP1 particles, we

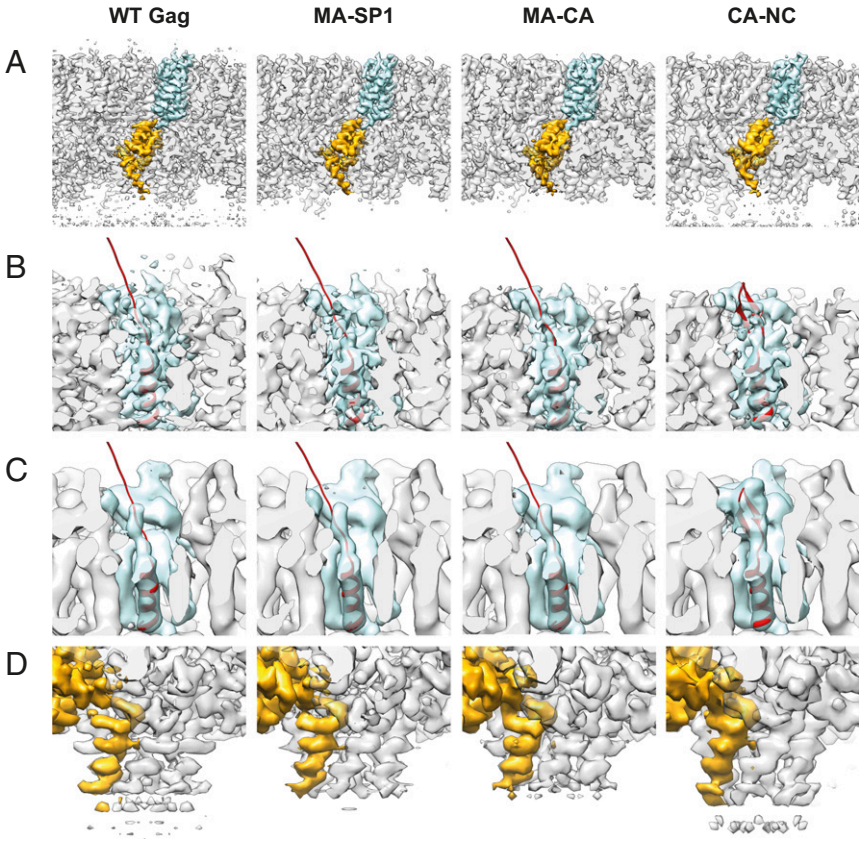

Fig. 3. Structure of the immature Gag CA layer. Isosurface representations of the structure of the immature Gag CA layer in each cleavage mutant, compared with the previously published wild-type (WT) immature structure (EMD-4017) (10). (*A*) View perpendicular to the lattice. One immature CA domain is highlighted in color for emphasis (cyan, CA-NTD; orange, CA-CTD). (*B*) Comparison of the density N-terminal to helix 1 in the CA-NTD density in each of the maps. In each case, PDB coordinates of helix 1 and its upstream linker (red) were rigid-body-docked into the density map. For WT Gag, MA-SP1, and MA-CA, model 4 from an NMR solution structure of MA-CA (PDB ID code 16LN) was used. For CA-NC, helix 1 and the upstream beta-hairpin from a mature CA crystal structure (PDB ID code 5HGK) were used. (*C*) As in *B*, but with density maps low-pass-filtered to 6 Å to more readily show the larger density upstream of helix 1 in CA-NC, consistent with the presence of a beta-hairpin. (*D*) Comparison of the CA-SP1 six-helix bundle density in each immature structure. The helical bundle in all structures appears to have the same length, ending at residue T371. Additional disordered density is visible downstream of the bundle in WT Gag and CA-NC, corresponding to the C-terminal part of SP1 and downstream residues.

determined 11 pentameric positions. All of these pentamers were detected in regions with high lattice curvature. The low number of pentameric positions compared with wild-type capsids reflects the fact that only incomplete polyhedral structures are seen for this variant, and that they have generally low overall curvature. For CA-NC, we identified 14 pentamers, again at positions of high curvature. For MA-CA particles, we identified only two pentamerically coordinated positions, which was insufficient for structure determination. For both CA-SP1 and CA-NC, we extracted subtomograms from pentamerically coordinated positions and iteratively averaged and aligned them as previously described (11) to generate low-resolution reconstructions of the CA pentamers (Fig. 5). An estimate of the resolution achieved was obtained by calculating the Fourier shell correlation (FSC) between the averages and the structure previously obtained for the HIV-1 wild-type pentamer (Electron Microscopy Data Bank accession code EMD-3466) (*SI Appendix*, Fig. S1*C*), resulting in 24 Å for CA-SP1 and 22 Å for CA-NC according to the 0.5 FSC criterion. Up to the determined resolutions, the structures of the pentamers from mutant particles were consistent with the structure of the wild-type pentamer.

Architecture of Immature and Mature CA Lattices. We next analyzed the architecture of the CA lattices within the variant particles in comparison to wild-type immature and mature particles. To do this, we visualized the global arrangement of the CA lattice using previously described "lattice maps" (9) (Fig. 6). For all variants, the arrangement of immature-like Gag lattices was generally consistent with what had been observed for wild-type particles: The lattices were hexameric and contained small gaps and imperfections as well as one larger gap in the lattice that likely corresponds to the site where budding occurred. The lattice maps also confirmed the observation made above based on visual analysis of the tomograms that for a small subset of MA-CA and MA-SP1 particles, there was no large gap and often no RNP (Fig. 2 *A*, *v* and *B*, *viii*).

Lattice maps derived from mature assemblies found in MA-CA, CA-NC, and CA-SP1 particles confirmed the morphological analyses described in the previous section. Of the 78 CA-SP1 particles containing mature lattices, three appeared to be almost closed structures with irregular morphology. The remaining 75 represented open, incomplete polyhedra, containing cracks and gaps as well as pentamerically coordinated positions (Fig. 6 *A*, *xxv*; *B*, *xxvi*; and *C*, *xxvii*).

In the case of the MA-CA variant, the extent of the lattice with mature morphology varied between particles. Consistent with CA being connected to the MA/membrane layer, the hexameric lattice displayed a low curvature following the viral envelope (Fig. 6 *A*, *xiii*; *B*, *xiv*; and *C*, *xv*). Cracks and gaps were detected in this lattice, similar to those observed in immature Gag lattices; these imperfections can relieve structural stress that would otherwise build up in a curved hexameric lattice. In contrast, pentamers were almost completely absent in these particles. Although we cannot exclude the possibility that the absence of the CA beta-hairpin inhibits pentamer formation in the MA-CA variant, we suggest that the absence of pentamers results from the lack of regions of high curvature in this case.

In CA-NC particles, mature lattices often formed irregular polyhedral cores more variable in morphology than those seen in wild-type mature viruses. From the 35 CA-NC virions displaying mature lattices, four of the virions contained two cores. Twenty-four of the 39 observed mature lattices formed irregular polyhedra, two appeared conical, and two appeared triangular. All of these phenotypes have previously been reported for wild-type mature cores (6, 7). The remaining mature lattices (11 of 39) formed open, curved sheets that were smaller in size than the more complete polyhedral cores.

Where immature and mature lattices were found in the same particle, they abutted each other (Fig. 6 *A*, *x* and *xix*; *B*, *xi* and *xx*; and *C*, *xii* and *xxi*). They were connected by a region of apparent local disorder, as suggested by lack of alignment/correspondence to either mature or immature CA references. Immature and mature

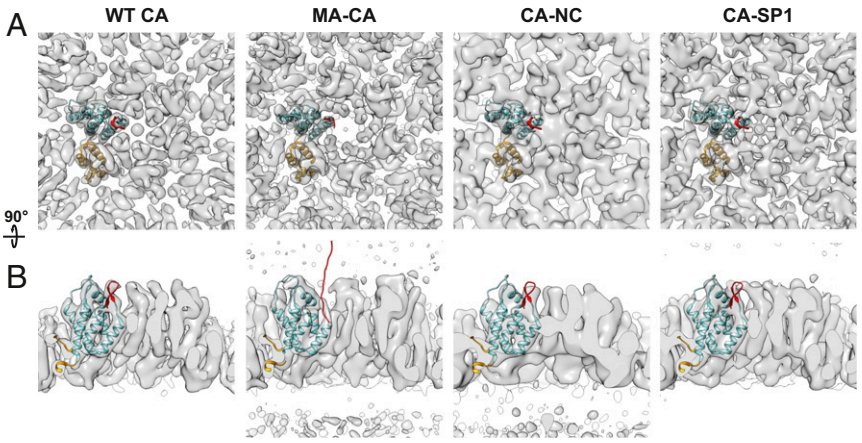

Fig. 4. Structure of the mature CA hexamer. Isosurface representations of the structure of the mature CA hexamer in each cleavage mutant, compared with the previously published wild-type (WT) CA hexamer structure (EMD-3465) (11). A structural model of mature CA with the beta-hairpin in the closed conformation (PDB ID code 5MCX) was rigid-body-docked into the electron densities for WT CA, CA-NC, and CA-SP1, with the CA-NTD shown in cyan, the CA-CTD shown in orange, and the beta-hairpin shown in red. For MA-CA, the CA-NTD is a separately docked NMR solution structure (PDB ID code 1L6N) that contains a linear MA-CA linker (red) instead of a beta-hairpin motif. The resolutions of the maps differ: WT CA, 6.8 Å; MA-CA, 8.3 Å; CA-NC, 9.7 Å; CA-SP1, 7.9 Å. (*A*) View of the lattice down its sixfold symmetry axis from the CA-NTD end. A density corresponding to the beta-hairpin is seen in WT CA, CA-NC, and CA-SP1, but not in MA-CA. (*B*) Rotation of 90° to view the hexamer viewed perpendicular to the CA lattice and cut open to better visualize the beta-hairpin and helix 1. The CA-SP1 six-helix bundle seen in the immature lattice is absent in the mature lattice, and no density was seen for residues 354–378.

lattices have also been found within the same particles after treatment with the maturation inhibitor PF-46396 (40), but these lattices do not abut each other. The close spatial proximity of the two lattice types in the cleavage mutants suggests that they are linked, either through interactions with the membrane via MA (for MA-CA) or through interactions with the RNP (for CA-NC).

Discussion

Formation of the wild-type, mature HIV-1 core requires maturation at three levels: (*i*) proteolytic maturation—correct processing by PR at all five sites in Gag, (*ii*) structural maturation—transition of the CA packing arrangement from an immature to mature CA lattice, and (*iii*) architectural maturation—transition from a truncated spherical immature Gag layer with irregular defects to a closed conical mature core with pentamers at the narrow and wide ends. Previous studies on viral cleavage site mutants (22, 25–32) have shown that interfering with the degree or rate of proteolytic cleavage at individual sites in Gag almost invariably leads to defects in the architectural transition manifested in irregular core shapes, incomplete cores, or empty cores that exclude the viral genome. Our observations here support and refine these results: We found that all variants with cleavage site mutations, and therefore defective in proteolytic maturation, were defective in architectural maturation. On the other hand, some variants with cleavage site mutations do support (partial) structural maturation of the CA lattice, thus shedding light on the regulation of this process.

Consistent with previous results (30), we observed that cleavage both upstream and downstream of the CA-SP1 module is sufficient for structural maturation of the CA lattice. Based on lower resolution structures from smaller datasets (30), we had previously concluded that cleavage both upstream and downstream of the CA or CA-SP1 lattice is necessary for structural maturation, but this interpretation needs to be revised based on the results presented here. Although predominantly immature, both MA-CA and CA-NC particles did contain regions of mature CA lattice, indicating that cleavage at both termini of CA is not essential for CA structural maturation. MA-SP1 particles, however, appeared to be entirely immature, suggesting that cleavage exclusively between CA and NC is only sufficient for structural maturation when it occurs between CA and SP1. These observations indicate that the relationship between proteolytic maturation and structural maturation is complex: There is no single cleavage site at which successful proteolytic cleavage is required for structural maturation; when any cleavage site between MA and NC is blocked by mutation, a combination of other cleavages can permit structural maturation, albeit at low efficiency.

There has been a debate in the field as to whether HIV-1 maturation proceeds by disassembly/reassembly or via a displacive transition. A fully displacive transition (i.e., direct transformation of the immature lattice into the mature lattice) (41) is inconsistent with the differences in the relative relationships and numbers of CA in the immature and mature lattices. We and others therefore prefer a model in which the lattice disassembles into smaller oligomers or patches, which undergo structural maturation, followed by assembly of the mature capsid architecture (20, 42). In the context of this model, the observed defects in architectural maturation in the MA-CA and CA-NC mutants can simply be caused by CA remaining tethered to MA or NC during structural maturation of the CA lattice. The architectural maturation defect observed for CA-SP1 suggests that dysregulation of disassembly kinetics can also lead to defects in mature lattice architecture. The observation of distinct and segregated patches of mature and immature lattices in both MA-CA and CA-NC mutants, as well as in particles treated with the maturation inhibitor PF-46396 (40), suggests that structural maturation occurs in a processive manner where the likelihood of maturation is increased by maturation of a neighboring hexamer. This could simply result from local destabilization of the structure by cleavage of neighboring molecules. We note that whether maturation is processive or stochastic has no bearing on whether it occurs via disassembly/reassembly or via a displacive transition.

We observed that the immature CA-NC lattice can accommodate the N-terminal beta-hairpin of CA. Conversely, MA-CA can form a mature CA lattice lacking the beta-hairpin, consistent with the ability of a construct lacking the N-terminal 12 residues of CA to assemble a mature CA lattice in vitro (43). These findings indicate that beta-hairpin formation is neither sufficient to destabilize the immature CA lattice nor required to assemble the mature lattice. This makes it unlikely that formation of the beta-hairpin is the switch controlling structural maturation of CA. Instead, it suggests that the hairpin may be functionally relevant after maturation rather than influencing the process of maturation itself. Conceivably, beta-hairpin formation may influence the properties of the adjacent central pore in the CA hexamer that appears to be important in early replication stages (44).

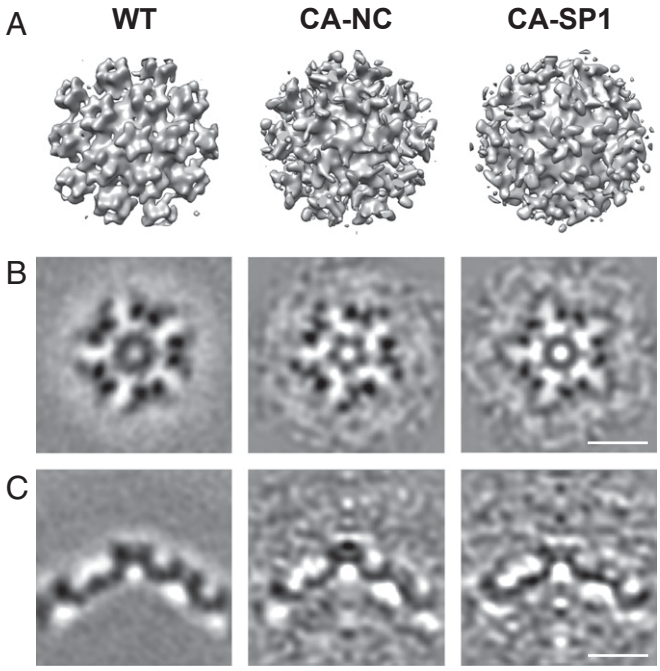

Fig. 5. Structure of the mature CA pentamer. Comparison between previously obtained wild-type (WT) CA pentamer structure (EMD-3466) and the CA-NC and CA-SP1 pentamer structures obtained here. (*A*) Isosurface representations of the mature pentamer maps in the WT virus and in the CA-NC and CA-SP1 cleavage mutants, viewed from outside the core. (*B*) Orthoslice of 5.4-Å thickness through each of the maps, viewed parallel to the plane of the pentamer. Although the resolution of the CA-NC and CA-SP1 pentamers is limited due to the very small number of subvolumes averaged, the overall pentamer structure in both of these mutants is similar to the WT CA pentamer, indicating that a CA pentamer is present. (*C*) Perpendicular orthoslice to the view in *B*, through the fivefold symmetry axis, showing the curvature of each pentamer. Scale bars, 10 nm.

In all immature lattice structures observed, the CA-SP1 bundle was intact and had the same length. Conversely, no helical density was visible downstream of the CA-CTD in any of the mature lattice structures, including that of CA-NC, indicating that the CA-SP1 region is disordered in all these cases. Consistent with these observations, in mature-like CA-SP1 tubes assembled in vitro, the predominant conformation is nonhelical and no six-helix bundle is present (45, 46). Destabilization of the CA-SP1 six-helix bundle therefore correlates with structural maturation of the CA domains, even in the absence of proteolytic cleavage at the CA/SP1 site.

In the MA-CA variant, partial cleavage takes place between CA and SP1. Since helix destabilization is required to allow PR to access the cleavage site, this implies that the CA-SP1 helix can undergo transient destabilization when CA remains tethered to MA, even though the six-helix bundle is predominantly present. In the MA-CA variant, PR cleavage makes the transient destabilization permanent, and some regions of mature CA lattice are therefore formed. In the MA-SP1 variant, cleavage between CA and SP1 cannot take place, and no regions of mature lattice are observed. Despite cleavage of a subset of CA-SP1 sites in the MA-CA variant, we do not see a structural change in the six-helix bundle in the immature lattice. We see three possible causes for this: (*i*) molecules that have been cleaved between CA and SP1 have undergone structural maturation and form part of the mature-like lattice in the mixed-phenotype particles, (*ii*) partially cleaved six-helix bundles largely retain their structural integrity, or (*iii*) complete cleavage of a subset of six-helix bundles does not destabilize the immature lattice. It is likely that a combination of these causes explains our observations.

Structural maturation involves resolution of interactions that stabilize the immature Gag lattice and formation of a stable, mature CA lattice. Destabilization of the immature lattice is a prerequisite for structural maturation. Several structural features contribute to stabilization of the immature lattice: (*i*) CA–CA interactions, (*ii*) interactions within the helical bundle formed at the CA-SP1 boundary, (*iii*) tethering of the CA lattice via C-terminal NC–RNA interactions, and (*iv*) tethering of the CA lattice by N-terminal MA–membrane interactions. Based on our results, we suggest that resolution of the CA-SP1 six-helix bundle represents the switch for structural maturation. This resolution could be achieved by removal of the tethering interactions to MA and/or NC, or by the transient formation of destabilizing interactions, for example, by formation of the beta-hairpin within the immature lattice. The observations that (*i*) no individual cleavage site is necessary for structural maturation and (*ii*) beta-hairpin formation does not correlate with structural maturation strongly argue against a role of transient destabilizing interactions. Instead, the immature lattice must be resolved by loss of stabilizing interactions, such as tethering via MA to the membrane and/or through NC to RNA. Loss of both of these tethers, as in the CA-SP1 variant, leads to destabilization of the six-helix bundle and structural maturation. Loss of the tether to MA leads to partial structural maturation, as does loss of the tether to NC in the MA-CA variant. Both of these tethers therefore contribute to stability of the immature lattice.

In summary, the data described here are consistent with a model in which integrity of the six-helix bundle within the immature CA lattice is maintained by the cumulative effects of multiple stabilizing interactions. Structural maturation is promoted by removing various subsets of these interactions through proteolytic cleavage, thereby destabilizing the bundle. In keeping with this model, maturation can be inhibited by stabilizing the helical form of SP1. This can be achieved by specific point mutations, such as threonine to isoleucine at position 8 in SP1 (47). Alternatively, treatment with maturation inhibitors, such as bevirimat, stabilizes the CA-SP1 bundle and also arrests the virus in an immature-like state (39). Accordingly, resistance against maturation inhibitors develops through mutations that destabilize the six-helix bundle and thereby counteract the stabilizing effect of the inhibitor, thus restoring the maturation switch (10, 17, 48, 49).

Materials and Methods

Particle Production and Purification. Virus-like particles were produced in HEK293T cells transfected with plasmids derived from pCHIV (50), which carried the indicated PR cleavage site mutations (29, 51). For this, cells seeded in 175-cm^2 flasks were transfected with 70 μg of plasmid per flask using a standard $CaPO_4$ transfection procedure. At 36 h posttransfection, tissue culture supernatants were harvested and filtered through 0.45-μm nitrocellulose, and particles were concentrated by ultracentrifugation through a 20% (wt/vol) sucrose cushion (2 h at 28,000 rpm in a Beckman SW32 rotor; Beckman Coulter Life Sciences). Particles were further purified by ultracentrifugation through an iodixanol gradient as described previously (52). Particle-containing fractions were diluted with PBS (1:8) and again concentrated by ultracentrifugation (30 min, 44,000 rpm in a Beckman SW60 rotor; Beckman Coulter Life Sciences). Particle pellets were gently resuspended in PBS, fixed with 1% paraformaldehyde for 1 h at 0 °C, and stored in aliquots at −80 °C.

Immunoblot Analysis. Particle lysates were separated by SDS/PAGE (200:1 acrylamide/bisacrylamide), and proteins were transferred to a nitrocellulose membrane by semidry blotting. Gag-derived proteins were detected by quantitative immunoblot analysis on a LI-COR Odyssey CLx infrared scanner (LI-COR Biotechnology) following the manufacturer's instructions, using rabbit polyclonal antiserum raised against recombinant HIV-1 CA and IRDye 800CW donkey anti-rabbit IgG secondary antibody (LI-COR Biotechnology). ImageStudio software (version 5.2; LI-COR Biotechnology) was used for generation of images and quantitation of band intensities.

Cryo-EM Sample Preparation. A solution of PBS containing 10-nm-diameter colloidal gold beads was added to a suspension of purified HIV-1 mutant particles with a final ratio, by volume, of 1:1 between the gold suspension

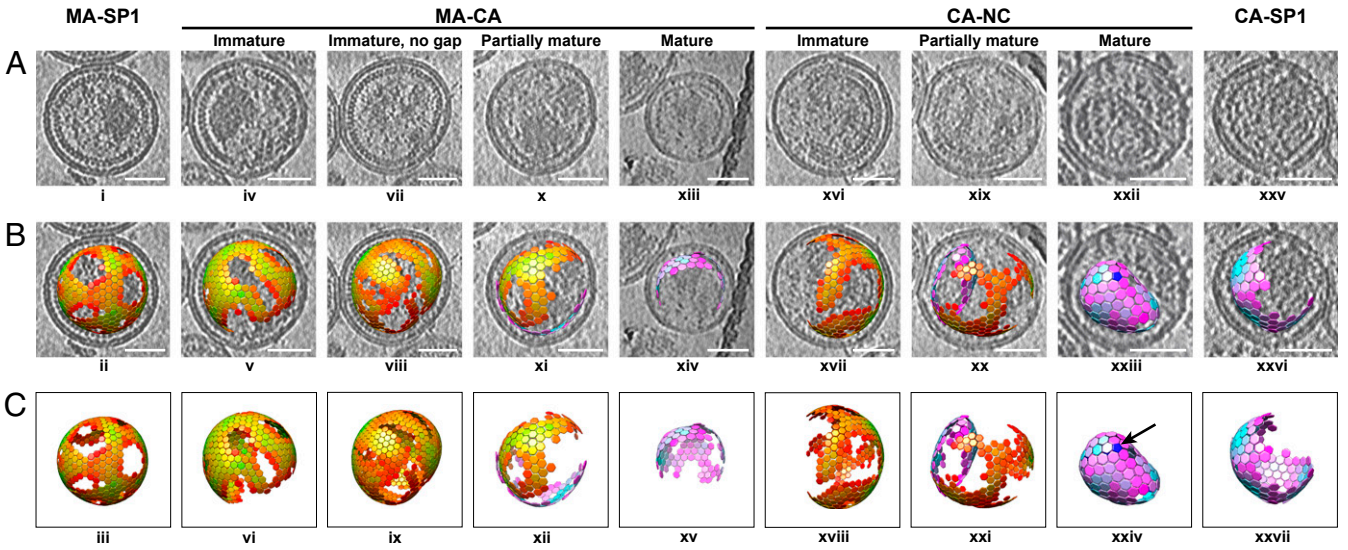

Fig. 6. (*A–C*, *i–xxvii*) Lattice map representations of aligned subtomograms used to generate the structures, illustrating the different viral morphologies observed in the samples. Scale bars, 50 nm. (*A*) Computational slices of 5.4-Å thickness through the tomogram to illustrate representative viruses for each morphology. (*B*) Lattice maps overlaid on the corresponding tomographic slice. Each hexagon or pentagon corresponds to a single subtomogram, centered on a CA domain hexamer or pentamer, respectively. These geometric objects are displayed at the coordinates and orientations of the center of each subvolume determined during alignment. They provide a representation of the arrangement of hexameric subunits in the immature lattice and of the hexameric and pentameric subunits in mature CA lattices. Immature hexamers are displayed on a color scale of red to green, from low to high CCC. A corresponding magenta-to-cyan color scale is used for mature hexamers. Mature pentamers are shown in blue. Only one pentamer is clearly visible in the illustrated lattice maps (arrow in *xxiv*). (*C*) Lattice maps displayed without the corresponding tomographic slice.

and viral suspension. A portion (2.5 μL) of the sample was applied to a C-Flat 2/2 3C grid previously glow-discharged at 20 mA for 30 s. Samples were blotted and plunge-frozen in liquid ethane using an FEI Vitrobot Mark II operated at 15 °C and 100% humidity. The grids were stored in liquid nitrogen until image acquisition.

Cryo-ET Tomography. Tomographic tilt series between −60° and +60° were acquired using a dose-symmetric tilt scheme (53), with a tilt increment of 3°, on an FEI Titan Krios transmission electron microscope at 300 kV in superresolution mode, equipped with a Gatan Quantum 967 LS energy filter with a slit width of 20 eV. Tilt series images were acquired on a Gatan K2xp detector with 10 frames per tilt and a total dose of ∼150 $e^{-}/Å^2$ across all of the tilts. Superresolution frames were aligned on-the-fly in SerialEM (54) and Fourier-cropped to 3,708 × 3,708 pixels, giving a final pixel size of 1.35 Å per pixel in the unbinned image stacks.

The tilt image stacks were sorted by tilt angle using IMOD (55), and exposure filtering was performed in MATLAB (MathWorks) using the formula described by Grant and Grigorieff (56). Contrast transfer function (CTF) determination was performed on the non–exposure-filtered stacks using CTFFIND4 (57). All tomograms were then reconstructed using IMOD with initial 2D CTF correction performed using the program "ctfphaseflip" (58). The final unbinned tomograms were also reconstructed again with 3D CTF correction on the input stacks by CTF multiplication in NovaCTF (59), with astigmatism correction and a strip size of 15 nm. The 3D CTF-corrected tomograms were used for the final step of unbinned subtomogram alignment (discussed below).

Image Processing: Immature Viruses. For the MA-SP1, MA-CA, and CA-NC datasets, the centers of immature viruses in 8× binned tomograms were marked manually using a custom plug-in for UCSF Chimera (60). An oversampled grid of initial extraction points was defined using MATLAB on a spherical surface centered on these positions, with a radius set appropriately for each virus. Subtomogram averaging and alignment were performed independently for each dataset using MATLAB scripts based on TOM (61), AV3 (62), and Dynamo (63) as previously described (10). For each dataset, viruses from one tomogram with high defocus (>4.0 μm) were chosen for construction of an initial reference.

For construction of initial references, subtomograms were extracted from 8× binned tomograms with a box size of $(389\ Å)^3$ and averaged. Iterative reference-free alignment was performed with a 6 × 4° conical search and 8 × 5° in-plane search. For MA-SP1, five iterations were performed while applying a 29.9-Å low-pass filter. For MA-CA and CA-NC, seven iterations were performed with a 32.4-Å low-pass filter. The average was shifted to center the sixfold symmetry axis in the box, and two further iterations of alignment were performed with the same parameters, but with a sixfold symmetrized reference. Subvolumes closer than 32.4 Å (four pixels) apart were removed from the dataset, along with those with a low cross-correlation coefficient (CCC), which did not contain Gag. For MA-SP1, one final iteration of alignment was then performed on the remaining subvolumes in the dataset, with a 4 × 1° cone search, 5 × 1° in-plane search, sixfold symmetry, and 29.9-Å low-pass filter. For MA-CA and CA-NC, three further iterations of angular search were performed with the same parameters as before and with sixfold symmetry. The resulting averages here were used as the initial references for each dataset.

For alignment of each full dataset against the respective reference, 2D CTF-corrected tomograms were used unless otherwise stated. Subtomograms were extracted from the full set of 8× binned tomograms as before. The respective reference was used for two iterations of alignment with a 7 × 6° angular search range for each Euler angle and a 32.4-Å low-pass filter. As before, points with a low CCC and those closer together than half the lattice spacing of 8 nm were then removed from the dataset. The positions and orientations of the points obtained from alignment of 8× binned subtomograms were then used for successive alignment using 4× binned, 2× binned, and then unbinned subtomograms using the same steps and parameters as previously described (10), with the data split into independent odd and even half-datasets after alignment of the 4× binned subtomograms.

For 3D CTF estimation and correction, after two iterations of alignment of unbinned subtomograms from 2D CTF-corrected tomograms, the positions of all points were used to calculate the center-of-mass for defocus estimation of each dataset. These values were used for reconstruction of the unbinned tomograms with 3D CTF correction as described above. Subtomograms with a box size of $(259\ Å)^3$ were then reextracted from the 3D CTF-corrected tomograms and averaged to produce new odd/even references for the half-datasets. A further iteration of alignment was run against these references with a 2 × 1° angular search for all Euler angles and a band-pass filter of 8.1–25.9 Å applied to the references during alignment. Image processing statistics are summarized in Table 2.

Image Processing: Mature Viruses. The approximate outlines of complete and incomplete mature cores were traced on X–Y slices through 8× binned tomograms of CA-NC viruses, using the segmentation function of Amira (versions 5.5 and 6.1.1; FEI). These paths were interpolated in Amira to produce a binary volume mask for each core, which was filtered with a

Table 2. Image processing statistics for all cleavage mutants

Structure determination	Sample					
	Immature HIV-1 MA-SP1	Immature HIV-1 MA-CA	Immature HIV-1 CA-NC	Mature HIV-1 MA-CA	Mature HIV-1 CA-SP1	Mature HIV-1 CA-NC
Gag/CA hexamer structure determination						
Viruses	352	368	338	37	74	29
Asymmetric units set A	265,716	231,492	159,444	10,314	23,988	5,844
Asymmetric units set B	265,728	231,450	159,174	10,320	23,994	5,940
Final resolution (0.143 FSC), Å	4.0	3.7	4.5	8.3	7.9	9.7
EMDB accession code	EMD-0164	EMD-0165	EMD-0166	EMD-0167	EMD-0169	EMD-0168
CA pentamer structure determination						
Asymmetric units	—	—	—	—	55	70
Final cross-resolution (0.5 FSC), Å	—	—	—	—	24	22
EMDB accession code	—	—	—	—	EMD-0171	EMD-0170

circular Gaussian kernel of 20 pixels in MATLAB using the "tom_filter" function of the TOM package and utilized to generate isosurfaces. Points with a spacing of two pixels were sampled along the isosurfaces at an intensity threshold of 0.3 and were assigned Euler angles based on their orientation relative to the normal of the surface at each point. The in-plane angle of each point was randomized between 0° and 360°.

For the CA-SP1 and MA-CA viruses containing mature lattices, initial extraction points along the mature CA lattice were defined in Amira (version 4.1.2), by marking the center and measuring the radius of a sphere matching the lattice curvature. Extraction points were generated in MATLAB as for the immature lattice, with a spacing of 2.16 nm (two pixels). Initial CA-SP1 and MA-CA references were constructed by extracting subtomograms from a single 8× binned tomogram from each dataset with a box size of $(691\ Å)^3$. For CA-NC, only a single viral core was used to generate the reference. Extracted subvolumes from each respective dataset were averaged, and reference-free alignment was run independently with a $2 \times 10°$ cone search, $18 \times 10°$ in-plane search, 49.4-Å low-pass filter, and no symmetry applied until each reference converged on a hexagonal lattice. Two further iterations of alignment with the same parameters were run, but with a manually determined threshold for exclusion of points with low CCC from the average. The references were shifted to center them on the sixfold symmetry axis of a CA hexamer, and each alignment reference was generated by running two iterations of alignment with a $5 \times 4°$ cone search, $5 \times 6°$ in-plane search, 49.4-Å low-pass filter, and sixfold symmetry.

The full CA-SP1 and MA-CA mature hexamer datasets were processed as follows. Initially sampled points, as described above, were used for extraction of subtomograms from 8× binned tomograms of each respective dataset. Subtomograms from each dataset were subjected to two initial iterations of alignment against the respective reference generated as above, with a $10 \times 4°$ cone search, $10 \times 3°$ in-plane search, 49.4-Å low-pass filter, and sixfold symmetry applied to the reference. Misaligned and duplicate points from oversampling were then removed from the dataset based on CCC and with a minimum pairwise distance threshold of 5.4 nm. For the CA-SP1 dataset, two more iterations of alignment were run after this cleaning step.

The full CA-NC dataset was processed differently due to the irregular surface shapes of its variable mature cores. All CA-NC alignments were run with sixfold symmetry applied to the reference. To correct for inaccuracies in the initial tracing of the CA-NC cores, subtomograms were extracted from 8× binned tomograms as for MA-CA and CA-SP1 and aligned along the *z* axis only against the reference for two iterations, with a $4 \times 10°$ cone search, $3 \times 10°$ in-plane search, and 49.4-Å low-pass filter. Subtomograms with low CCC were removed, and remaining points were converted into a UCSF Chimera marker set. Each marker set was overlaid on the corresponding tomogram in UCSF Chimera, and gaps in the lattice of points were filled using the Volume Tracer tool if necessary. These marker sets were read into MATLAB and used to generate an isosurface for resampling as before. Using the new surfaces, subtomograms were extracted from 8× binned tomograms and aligned as before. After cleaning based on distance and CCC as before, the subtomograms were subjected to two further iterations of alignment with a $4 \times 5°$ cone search and $5 \times 6°$ in-plane search.

For all mature datasets, after alignment from 8× binned data, subtomograms were extracted with a box size of $(346\ Å)^3$ from 4× binned tomograms at the aligned positions and averaged to produce a reference, against which the subtomograms were aligned for three iterations with a $4 \times 6°$ search for each Euler angle and a low-pass filter of 34.6 Å. Subtomograms were then extracted from 2× binned tomograms with a box size of $(346\ Å)^3$, and those with gray values more than ±1 SD from the mean (which may contain artifacts from gold beads) were removed. The remaining subtomograms were split into separate odd/even half-datasets and averaged to produce odd/even alignment references. Subtomograms in each half-dataset were aligned against the respective reference over two iterations with a $3 \times 2°$ search for all Euler angles and a low-pass filter of 24.7 Å. The positions from these alignments were used to extract subtomograms of $(346\ Å)^3$ from the unbinned tomograms, which were averaged to produce new odd/even references. One iteration of alignment with a $3 \times 1°$ angular search for all Euler angles and 15.3-Å low-pass filter was run, followed by one iteration of alignment with a $2 \times 1°$ angular search for all Euler angles and bandpass filter of 13–20 Å. Aligned subtomograms were then extracted from the unbinned 3D CTF-corrected tomograms and averaged to produce new references, which were used to repeat the last alignment iteration.

Visualization of Structures and Maps. Immature CA lattices were analyzed by fitting the central monomer from PDB ID code 5L93 as a rigid body using UCSF Chimera. Mature CA lattices were analyzed equivalently, fitting a monomer from PDB ID code 4XFX. To compare the CA-NTD density with structures with and without a beta-hairpin, we fit PDB ID code 5HGK and PDB ID code 1L6N (model 4) as rigid bodies.

Isosurface renderings of each final electron density map were produced using UCSF Chimera, as were orthoslices of the final pentamer structures obtained from 4× binned data. The fit of the immature Gag atomic model (PDB ID code 5L93) into each of the immature cleavage mutant hexamer maps was visualized using PyMOL (version 1.8.6.0; Schrödinger, LLC). The wild-type pentamer is visualized using a structure obtained from 4× binned data to facilitate a direct comparison. Orthoslices of viruses, as shown in the morphology figures, were generated by applying a 3D Gaussian filter with a five-pixel kernel to 4× binned tomograms in MATLAB and were rendered at a thickness of 5.4 Å in UCSF Chimera.

The positions and orientations of aligned subtomograms were visualized using lattice maps, which consist of an appropriate geometric object placed at the coordinates of each subtomogram box center, and rotated by the Euler angles found by subtomogram alignment. To visualize lattice morphology (Fig. 6 *B* and *C*), we used the coordinates from the 8× binned alignments after cleaning based on distance and CCC. The CCC threshold for visualization was set per virus such that only the subset of clearly misaligned subtomograms (those with translations or rotations that shifted/rotated them away from any underlying CA protein layer) was excluded. This ensured that the lattice maps were as complete as possible. We then manually excluded a small number of subtomograms that were retained above the CCC threshold but that, by visual inspection, were clearly misaligned or were not continuous with any region of hexameric lattice. For particles containing both immature and mature lattices, alignments with mature and immature references were considered independently. The references are sufficiently distinct that we did not identify positions at which subtomograms aligned to both references. All lattice map analysis was performed using a custom plug-in for UCSF Chimera.

Data Availability. The structures described in this paper have been deposited in the Electron Microscopy Data Bank (www.ebi.ac.uk/pdbe/emdb) under accession codes EMD-0164–EMD-0171 (Table 2).

ACKNOWLEDGMENTS. We thank D. Morado and B. Turoňová for computational assistance; W. Hagen for support during EM data collection; and K. Qu, F. Schur, Y. Bykov, and M. Anders-Össwein for discussion and technical assistance. This study was supported by Deutsche Forschungsgemeinschaft Grants BR 3635/2-1 (to J.A.G.B.), KR 906/7-1 and KR906/8-1 (to H.-G.K.), and MU 885/5-1 (to B.M.); the European Molecular Biology Laboratory (EMBL) (J.A.G.B.); and Medical Research Council Grant MC_UP_1201/16 (to J.A.G.B.). This study was technically supported by the EMBL IT Services unit.

1. Briggs JAG, Kräusslich H-G (2011) The molecular architecture of HIV. *J Mol Biol* 410: 491–500.
2. Sundquist WI, Kräusslich H-G (2012) HIV-1 assembly, budding, and maturation. *Cold Spring Harb Perspect Med* 2:a006924.
3. Bell NM, Lever AML (2013) HIV Gag polyprotein: Processing and early viral particle assembly. *Trends Microbiol* 21:136–144.
4. Freed EO (2015) HIV-1 assembly, release and maturation. *Nat Rev Microbiol* 13: 484–496.
5. Mattei S, Schur FK, Briggs JA (2016) Retrovirus maturation-an extraordinary structural transformation. *Curr Opin Virol* 18:27–35.
6. Benjamin J, Ganser-Pornillos BK, Tivol WF, Sundquist WI, Jensen GJ (2005) Three-dimensional structure of HIV-1 virus-like particles by electron cryotomography. *J Mol Biol* 346:577–588.
7. Briggs JAG, et al. (2006) The mechanism of HIV-1 core assembly: Insights from three-dimensional reconstructions of authentic virions. *Structure* 14:15–20.
8. Wright ER, et al. (2007) Electron cryotomography of immature HIV-1 virions reveals the structure of the CA and SP1 Gag shells. *EMBO J* 26:2218–2226.
9. Briggs JAG, et al. (2009) Structure and assembly of immature HIV. *Proc Natl Acad Sci USA* 106:11090–11095.
10. Schur FKM, et al. (2016) An atomic model of HIV-1 capsid-SP1 reveals structures regulating assembly and maturation. *Science* 353:506–508.
11. Mattei S, Glass B, Hagen WJH, Kräusslich H-G, Briggs JAG (2016) The structure and flexibility of conical HIV-1 capsids determined within intact virions. *Science* 354: 1434–1437.
12. Hill CP, Worthylake D, Bancroft DP, Christensen AM, Sundquist WI (1996) Crystal structures of the trimeric human immunodeficiency virus type 1 matrix protein: Implications for membrane association and assembly. *Proc Natl Acad Sci USA* 93: 3099–3104.
13. Gamble TR, et al. (1996) Crystal structure of human cyclophilin A bound to the amino-terminal domain of HIV-1 capsid. *Cell* 87:1285–1294.
14. Gamble TR, et al. (1997) Structure of the carboxyl-terminal dimerization domain of the HIV-1 capsid protein. *Science* 278:849–853.
15. Ganser-Pornillos BK, Yeager M, Sundquist WI (2008) The structural biology of HIV assembly. *Curr Opin Struct Biol* 18:203–217.
16. Gres AT, et al. (2015) X-ray crystal structures of native HIV-1 capsid protein reveal conformational variability. *Science* 349:99–103.
17. Wagner JM, et al. (2016) Crystal structure of an HIV assembly and maturation switch. *eLife* 5:e17063.
18. Briggs JAG, Wilk T, Welker R, Kräusslich H-G, Fuller SD (2003) Structural organization of authentic, mature HIV-1 virions and cores. *EMBO J* 22:1707–1715.
19. Briggs JAG, et al. (2004) The stoichiometry of Gag protein in HIV-1. *Nat Struct Mol Biol* 11:672–675.
20. Schur FKM, et al. (2015) Structure of the immature HIV-1 capsid in intact virus particles at 8.8 Å resolution. *Nature* 517:505–508.
21. von Schwedler UK, et al. (1998) Proteolytic refolding of the HIV-1 capsid protein amino-terminus facilitates viral core assembly. *EMBO J* 17:1555–1568.
22. Accola MA, Höglund S, Göttlinger HG (1998) A putative α-helical structure which overlaps the capsid-p2 boundary in the human immunodeficiency virus type 1 Gag precursor is crucial for viral particle assembly. *J Virol* 72:2072–2078.
23. Pettit SC, Lindquist JN, Kaplan AH, Swanstrom R (2005) Processing sites in the human immunodeficiency virus type 1 (HIV-1) Gag-Pro-Pol precursor are cleaved by the viral protease at different rates. *Retrovirology* 2:66.
24. Könnyű B, et al. (2013) Gag-Pol processing during HIV-1 virion maturation: A systems biology approach. *PLOS Comput Biol* 9:e1003103.
25. Göttlinger HG, Sodroski JG, Haseltine WA (1989) Role of capsid precursor processing and myristoylation in morphogenesis and infectivity of human immunodeficiency virus type 1. *Proc Natl Acad Sci USA* 86:5781–5785.
26. Kräusslich HG, Fäcke M, Heuser AM, Konvalinka J, Zentgraf H (1995) The spacer peptide between human immunodeficiency virus capsid and nucleocapsid proteins is essential for ordered assembly and viral infectivity. *J Virol* 69:3407–3419.
27. Wiegers K, et al. (1998) Sequential steps in human immunodeficiency virus particle maturation revealed by alterations of individual Gag polyprotein cleavage sites. *J Virol* 72:2846–2854.
28. Lee S-K, Harris J, Swanstrom R (2009) A strongly transdominant mutation in the human immunodeficiency virus type 1 gag gene defines an Achilles heel in the virus life cycle. *J Virol* 83:8536–8543.
29. Müller B, et al. (2009) HIV-1 Gag processing intermediates trans-dominantly interfere with HIV-1 infectivity. *J Biol Chem* 284:29692–29703.
30. de Marco A, et al. (2010) Structural analysis of HIV-1 maturation using cryo-electron tomography. *PLoS Pathog* 6:e1001215.
31. Checkley MA, Luttge BG, Soheilian F, Nagashima K, Freed EO (2010) The capsid-spacer peptide 1 Gag processing intermediate is a dominant-negative inhibitor of HIV-1 maturation. *Virology* 400:137–144.
32. de Marco A, et al. (2012) Role of the SP2 domain and its proteolytic cleavage in HIV-1 structural maturation and infectivity. *J Virol* 86:13708–13716.
33. Ehrlich LS, Agresta BE, Carter CA (1992) Assembly of recombinant human immunodeficiency virus type 1 capsid protein in vitro. *J Virol* 66:4874–4883.
34. Campbell S, Vogt VM (1995) Self-assembly in vitro of purified CA-NC proteins from Rous sarcoma virus and human immunodeficiency virus type 1. *J Virol* 69:6487–6497.
35. Gross I, Hohenberg H, Kräusslich H-G (1997) In vitro assembly properties of purified bacterially expressed capsid proteins of human immunodeficiency virus. *Eur J Biochem* 249:592–600.
36. Wan W, Briggs JAG (2016) Cryo-electron tomography and subtomogram averaging. *Methods Enzymol* 579:329–367.
37. Carlson L-A, et al. (2008) Three-dimensional analysis of budding sites and released virus suggests a revised model for HIV-1 morphogenesis. *Cell Host Microbe* 4:592–599.
38. Carlson L-A, et al. (2010) Cryo electron tomography of native HIV-1 budding sites. *PLoS Pathog* 6:e1001173.
39. Keller PW, Adamson CS, Heymann JB, Freed EO, Steven AC (2011) HIV-1 maturation inhibitor bevirimat stabilizes the immature Gag lattice. *J Virol* 85:1420–1428.
40. Keller PW, et al. (2013) A two-pronged structural analysis of retroviral maturation indicates that core formation proceeds by a disassembly-reassembly pathway rather than a displacive transition. *J Virol* 87:13655–13664.
41. Frank GA, et al. (2015) Maturation of the HIV-1 core by a non-diffusional phase transition. *Nat Commun* 6:5854.
42. Ning J, et al. (2016) In vitro protease cleavage and computer simulations reveal the HIV-1 capsid maturation pathway. *Nat Commun* 7:13689.
43. Gross I, Hohenberg H, Huckhagel C, Kräusslich H-G (1998) N-Terminal extension of human immunodeficiency virus capsid protein converts the in vitro assembly phenotype from tubular to spherical particles. *J Virol* 72:4798–4810.
44. Jacques DA, et al. (2016) HIV-1 uses dynamic capsid pores to import nucleotides and fuel encapsidated DNA synthesis. *Nature* 536:349–353.
45. Li S, Hill CP, Sundquist WI, Finch JT (2000) Image reconstructions of helical assemblies of the HIV-1 CA protein. *Nature* 407:409–413.
46. Wang M, et al. (2017) Quenching protein dynamics interferes with HIV capsid maturation. *Nat Commun* 8:1779.
47. Fontana J, et al. (2015) Identification of an HIV-1 mutation in spacer peptide 1 that stabilizes the immature CA-SP1 lattice. *J Virol* 90:972–978.
48. Adamson CS, et al. (2006) In vitro resistance to the human immunodeficiency virus type 1 maturation inhibitor PA-457 (Bevirimat). *J Virol* 80:10957–10971.
49. Waki K, et al. (2012) Structural and functional insights into the HIV-1 maturation inhibitor binding pocket. *PLoS Pathog* 8:e1002997.
50. Lampe M, et al. (2007) Double-labelled HIV-1 particles for study of virus-cell interaction. *Virology* 360:92–104.
51. Konvalinka J, et al. (1995) An active-site mutation in the human immunodeficiency virus type 1 proteinase (PR) causes reduced PR activity and loss of PR-mediated cytotoxicity without apparent effect on virus maturation and infectivity. *J Virol* 69: 7180–7186.
52. Dettenhofer M, Yu X-F (1999) Highly purified human immunodeficiency virus type 1 reveals a virtual absence of Vif in virions. *J Virol* 73:1460–1467.
53. Hagen WJH, Wan W, Briggs JAG (2017) Implementation of a cryo-electron tomography tilt-scheme optimized for high resolution subtomogram averaging. *J Struct Biol* 197:191–198.
54. Mastronarde DN (2005) Automated electron microscope tomography using robust prediction of specimen movements. *J Struct Biol* 152:36–51.
55. Kremer JR, Mastronarde DN, McIntosh JR (1996) Computer visualization of three-dimensional image data using IMOD. *J Struct Biol* 116:71–76.
56. Grant T, Grigorieff N (2015) Measuring the optimal exposure for single particle cryo-EM using a 2.6 Å reconstruction of rotavirus VP6. *eLife* 4:e06980.
57. Rohou A, Grigorieff N (2015) CTFFIND4: Fast and accurate defocus estimation from electron micrographs. *J Struct Biol* 192:216–221.
58. Xiong Q, Morphew MK, Schwartz CL, Hoenger AH, Mastronarde DN (2009) CTF determination and correction for low dose tomographic tilt series. *J Struct Biol* 168: 378–387.
59. Turoňová B, Schur FKM, Wan W, Briggs JAG (2017) Efficient 3D-CTF correction for cryo-electron tomography using NovaCTF improves subtomogram averaging resolution to 3.4Å. *J Struct Biol* 199:187–195.
60. Pettersen EF, et al. (2004) UCSF Chimera–A visualization system for exploratory research and analysis. *J Comput Chem* 25:1605–1612.
61. Nickell S, et al. (2005) TOM software toolbox: Acquisition and analysis for electron tomography. *J Struct Biol* 149:227–234.
62. Förster F, Medalia O, Zauberman N, Baumeister W, Fass D (2005) Retrovirus envelope protein complex structure in situ studied by cryo-electron tomography. *Proc Natl Acad Sci USA* 102:4729–4734.
63. Castaño-Díez D, Kudryashev M, Arheit M, Stahlberg H (2012) Dynamo: A flexible, user-friendly development tool for subtomogram averaging of cryo-EM data in high-performance computing environments. *J Struct Biol* 178:139–151.